

## ARTICLE OPEN



# Pre-oxidized ultramicroporous carbon cloth with ultrahigh volumetric capacity and ultralong lifespan for capacitive desalination

Xinyuan Zhao<sup>1</sup>, Yongshuo Zheng<sup>1</sup>, Zhilong Zheng<sup>2</sup>, Zhizhong Guo<sup>1</sup>, Tulai Sun<sup>3</sup>, Jiayi Qin<sup>1</sup>, Na Qiu<sup>1</sup>, Zhenyu Zhang<sup>4</sup> and Wei Wen<sup>1</sup>✉

Capacitive deionization is a promising desalination technique to tackle with freshwater scarcity, due to its facile, energy-efficient and eco-friendly operation. Carbon materials are primary electrode materials in capacitive deionization devices; however, their practical applications are limited by the low salt adsorption capacity and poor cycling stability. Here, we report a pre-oxidized strategy to significantly improve the salt adsorption capacity and cycling lifespan of carbon clothes. By the simple pre-oxidation treatment, it creates abundant ultramicropores and a superhydrophilic surface, which lead to a high salt adsorption capacity ( $31.5 \text{ mg g}^{-1}$  and  $13 \text{ mg cm}^{-3}$ ) in  $0.01 \text{ M NaCl}$  aqueous solution. Moreover, the surface of each carbon fiber is oxidized, combined with a high mechanical strength, resulting in a stable surface during the cycling process. The retention rate is 74% even after 5000 adsorption/desorption cycles in diluted seawater. This work provides a new avenue to the design of high-performance, low-cost, and durable electrodes for capacitive deionization applications.

*npj Clean Water* (2023)6:71 | <https://doi.org/10.1038/s41545-023-00289-z>

## INTRODUCTION

Freshwater scarcity is one of the most serious issues due to environmental pollution and rapid population growth<sup>1–3</sup>. Desalination of seawater or saline water is a sustainable technology to address the freshwater shortage, owing to a vast amount of seawater and brine water. The commercial desalination techniques mainly include reverse osmosis and thermal distillation, but they are energy intensive and costly, especially for the water with low salt concentrations (typically lower than  $1000 \text{ mg L}^{-1}$ )<sup>4–7</sup>. Alternatively, capacitive deionization (CDI) based on supercapacitor mechanisms is a promising desalination strategy because of its facile, energy-efficient and eco-friendly operation<sup>8–12</sup>. Carbon materials, including activated carbon, mesoporous carbon, carbon nanotubes, graphene, and carbon aerogel, are primary electrode materials in a typical CDI system<sup>13,14</sup>. However, the practical applications of conventional CDI are limited by the low salt adsorption capacity (typically  $0.1–15 \text{ mg g}^{-1}$ ) and poor cycling stability (usually below 100 cycles)<sup>15–18</sup>.

Although battery deionization exhibits high salt adsorption capacity<sup>19–22</sup>, the salt removals are selective, which is not suitable for treating water with complex components such as seawater. It is noticed that ultramicropores with a size less than 1 nanometer lead to the anomalous increase in carbon capacitances<sup>23,24</sup>. It was recently reported that ultramicropores also endow carbon materials with high deionization capacities even at seawater-level high salinity<sup>25</sup>. Apart from the gravimetric salt adsorption capacity (g-SAC) per unit mass, the volumetric salt adsorption capacity (v-SAC) per unit volume is another key figure-of-merit<sup>26,27</sup>. Porous carbons with large specific surface area contribute significantly to g-SAC, but the v-SACs are usually at a lower level because of the low density. In this regard,

ultramicroporous materials can obtain high specific surface area and high density simultaneously, due to the minimized pore space waste. Furthermore, it is expected that free-standing three-dimensional (3D) materials can maximize electrode capacity via avoiding the use of any inactive materials (current collectors, binders, and conductive agents).

Cycling lifespan critically impacts system viability in practical applications, as electrode degradation increases the desalination costs<sup>28,29</sup>. There is also a trade-off between salt adsorption capacity and cycling lifespan<sup>29</sup>. It is generally believed that the oxidation of carbon anode contributes to the diminishing desalination performance during cycling tests, because anode oxidation leads to a positive shift in its potential of zero charge, electrode resistance increase, and pore blockage<sup>29–32</sup>. Moreover, high mechanical strength is essential for prolonged use as well. Now it is highly urgent yet challenging to achieve a CDI electrode with high adsorption capacity (v-SAC and g-SAC), long cycling lifespan, and low-cost activation process.

Herein, we demonstrate a pre-oxidized strategy to significantly improve the CDI cycling lifespan and salt adsorption capacity. By a simple pre-oxidation of the carbon cloth in air (Fig. 1a), the surface of each carbon fiber is oxidized, leading to a more stable surface during the cycling process (Fig. 1b); whilst the interior of each carbon fiber still keeps the initial state to ensure low electric resistance, unlike the high interparticle resistance after the surface oxidation of particles in power-based electrodes. The surface pre-oxidation process also creates abundant ultramicropores and a superhydrophilic surface, which are instrumental in high salt adsorption capacity. Therefore, the pre-oxidized ultramicroporous carbon cloth exhibits ultrahigh salt adsorption capacity and ultralong lifespan.

<sup>1</sup>School of Mechanical and Electrical Engineering, Collaborative Innovation Center of Ecological Civilization, Hainan University, Haikou 570228, China. <sup>2</sup>Zhanjiang Power Supply Bureau of Guangdong Power Grid Co., Ltd., Zhanjiang 524001, China. <sup>3</sup>Center for Electron Microscopy, State Key Laboratory Breeding Base of Green Chemistry Synthesis Technology and College of Chemical Engineering, Zhejiang University of Technology, Hangzhou 310014, China. <sup>4</sup>Key Laboratory for Precision and Non-Traditional Machining Technology of Ministry of Education, Dalian University of Technology, Dalian 116024, China. ✉email: [wwen@hainanu.edu.cn](mailto:wwen@hainanu.edu.cn)

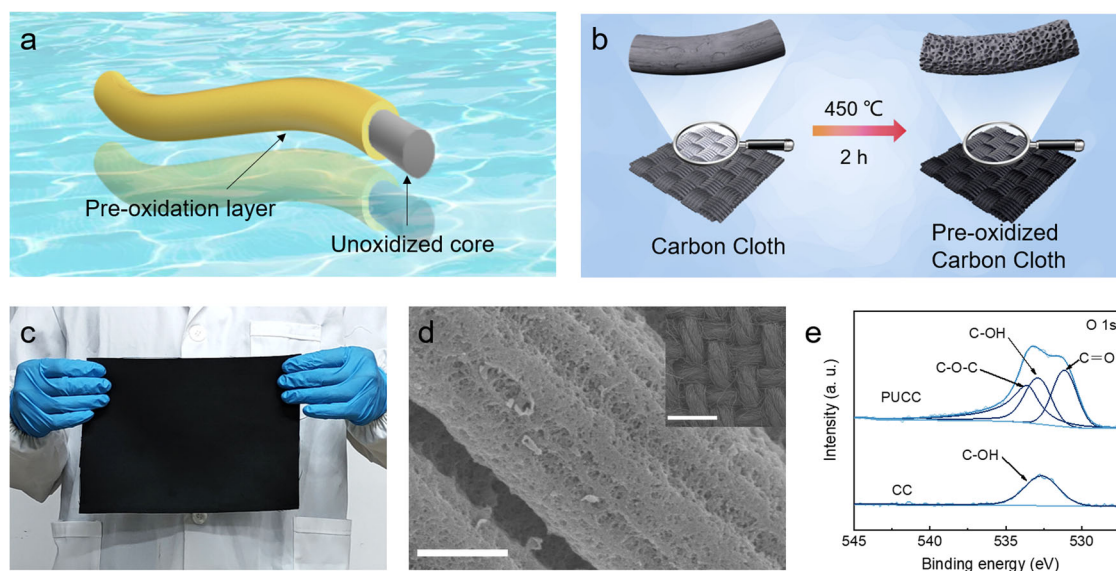


**Fig. 1 Schematics and structural characterizations of PUCC.** **a** Schematic diagram of carbon cloth fibers wrapped in a pre-oxide layer. **b** Schematic illustration of the preparation procedure of the PUCC. **c** Optical photograph and **(d)** FESEM image of PUCC. The scale bars in **(d)** and the inset are 1  $\mu\text{m}$  and 1 mm, respectively. **e** O 1s XPS spectrum of PUCC and CC.

## RESULTS

### Synthesis and characterizations

The pre-oxidized strategy is very simple and facile, which is suitable for mass production (Fig. 1b, c). Compared with the smooth surface of the untreated carbon cloth (labeled as CC, Supplementary Fig. 1), the pre-oxidized ultramicroporous carbon cloth (denoted as PUCC) exhibits a rough surface and porous structures (Fig. 1d and Supplementary Fig. 2). As shown in Supplementary Fig. 3, the diffraction peaks at  $25.0^\circ$  and  $43.5^\circ$  in the CC and PUCC can be indexed to hexagonal graphite with poorly crystallized structures. The peak intensity of the PUCC is weaker than that of the CC, suggesting the reduced carbon crystallinity after the pre-oxidized process. Raman spectroscopy was used to further probe the disorder degree in these two carbon materials by comparing the ratio of the disorder-induced band (D band at  $1350\text{ cm}^{-1}$ ) and graphite band (G band at  $1582\text{ cm}^{-1}$ ). The  $I_D/I_G$  ratio increases from 1.61 to 2.02 after the pre-oxidized process (Supplementary Fig. 4), verifying an enhanced surface disordering. In addition, the pre-oxidized strategy results in the surface oxidation of the carbon material. By X-ray photoelectron spectroscopy (XPS) measurement, the PUCC exhibits an enhanced O 1s signal when compared with the CC (Fig. 1e). The O 1s spectrum can be deconvoluted into three peaks corresponding to the C–OH, C–O–C, and C=O groups<sup>33,34</sup>, while there is only one peak corresponding to C–OH for the CC. As expected, the oxidation degree of the PUCC declines from the surface to the interior (Supplementary Fig. 5).

The pre-oxidized process also creates porous structures. The pore structures were further analyzed by  $\text{N}_2$  and  $\text{CO}_2$  adsorption/desorption experiments (Fig. 2a–c). Low-temperature  $\text{N}_2$  adsorption/desorption isotherms (Fig. 2a) shows a Type I shape, where the sharp increase of adsorption capacity in the low-pressure region corresponds to the typical characteristic of microporous materials. As shown in Fig. 2c, the width of the micropores mainly ranges from 0.4 to 1.0 nm, demonstrating an ultramicroporous feature. The specific surface area of the micropores in the PUCC is determined to be  $355\text{ m}^2\text{ g}^{-1}$  by the low-temperature  $\text{N}_2$  adsorption/desorption test, which is consistent with that obtained by the  $\text{CO}_2$  adsorption measurement ( $334\text{ m}^2\text{ g}^{-1}$ ). On the contrary, the CC shows a micropore-free characteristic. Additionally, the pore sizes measured by  $\text{N}_2$  are consistent with the  $\text{CO}_2$

adsorption measure (Fig. 2b, c), which further verifies the existence of ultramicropores. Although there are abundant ultramicropores in the PUCC, the tensile strength is close to that of the CC, whilst the Young's modulus is reduced (Fig. 2d). This tensile strength (2.6 MPa) is much higher than other free-standing carbon materials, such as 3D graphene ( $0.068\text{ MPa}$ )<sup>35</sup>. The high mechanical strength is also advantageous to obtain long cycling life.

Due to the surface pre-oxidation and the formation of ultramicropores, the electrical resistivity increases (from 1820 to  $4310\ \mu\Omega\text{ m}$ , Fig. 2e). Interestingly, the Seebeck coefficient and power factor increase by 30 and 322 times, respectively (Fig. 2e, f), which further affirm surface oxidation of carbon materials during the activation process<sup>36</sup>. Like other carbon fiber fabrics, the CC shows a hydrophobic characteristic, where water droplets gather on the surface, as shown in Fig. 2g. After the pre-oxidized process, the PUCC is superhydrophilic (Fig. 2h). As shown in Fig. 2i, j, the contact angle for the CC was determined to be  $143^\circ$ , while the water droplet rapidly permeates the PUCC once it touches the surface.

### Electrochemical performances

The high surface area, superhydrophilic surface and ultramicroporous characteristic of the PUCC make it an ideal electrode for CDI, without the need for additional conductive additives and binders. The basic electrochemical performances of the PUCC in a standard three electrode system were measured in NaCl aqueous solution before using it as an electrode for CDI. The counter electrode was platinum and the reference electrode is Ag/AgCl electrode. The PUCC shows a nearly rectangular shape for the cyclic voltammetry (CV) curves at  $1\text{--}10\text{ mV s}^{-1}$  when being used as an anode ( $-1$  to  $0\text{ V}$  vs. Ag/AgCl, Fig. 3a), which indicates that the formation of efficient electrochemical double layers (EDLs) and fast ion transport across the PUCC.

Thanks to the EDL-based mechanisms, the PUCC can also serve as a cathode (Fig. 3b). The capacities of the PUCC as anode are slightly higher than those as cathode (Fig. 3a, b), which can be attributed to the negative charge on the surface of the PUCC at neutral pH (Supplementary Fig. 6). The PUCC can function as both anode and cathode to assemble a symmetric full cell. The rectangular shape for the CV curves (Fig. 3c) and the nearly

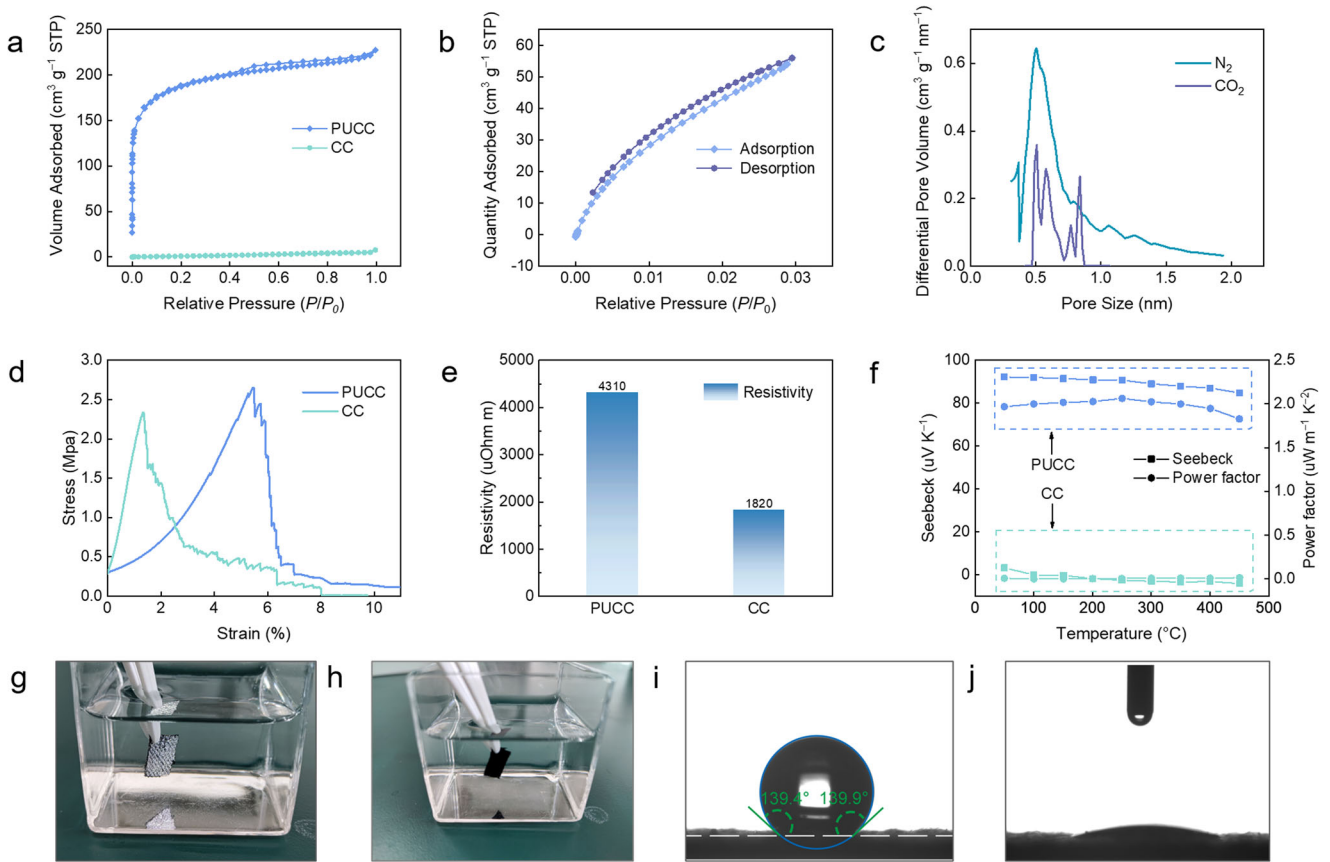


**Fig. 2** The characterizations of PUCC and CC. **a** Low-temperature  $\text{N}_2$  adsorption/desorption isotherms of PUCC and CC. **b**  $\text{CO}_2$  adsorption/desorption isotherms of PUCC. **c** The pore size distributions of PUCC. **d** Strain-stress curves of PUCC and CC. **e** Resistivity of PUCC and CC at room temperature. **f** Schematic diagram of Seebeck coefficient and power factor of PUCC and CC at different temperatures (50–450  $^{\circ}\text{C}$ ). The phenomena for CC (**g**) and PUCC (**h**) immersed in water. Contact angle measurements for CC (**i**) and PUCC (**j**).

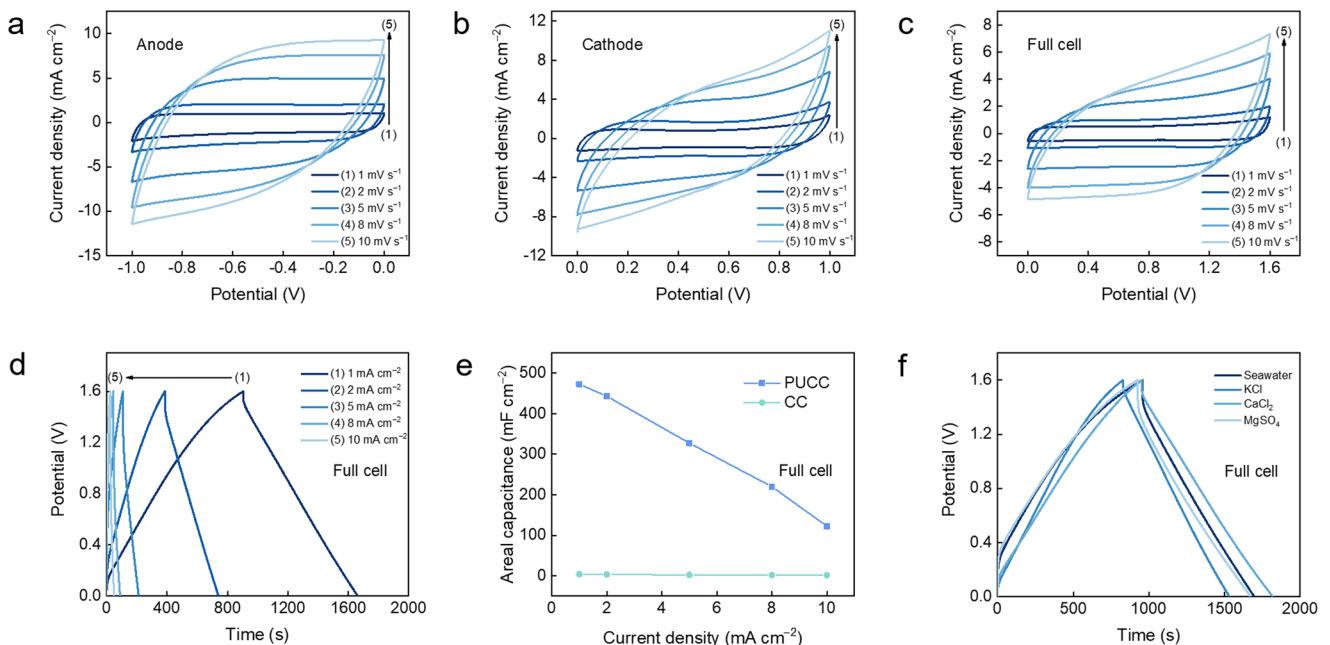


**Fig. 3** Electrochemical performances of PUCC. **a** CV curves of PUCC at scan rates from 1 to 10  $\text{mV s}^{-1}$  as anode (**a**) and cathode (**b**). CV curves (**c**) and galvanostatic charge/discharge curves (**d**) of the full cell assembled by two PUCCs. **e** Areal specific capacitances for PUCC and CC in the full cells. **f** Galvanostatic charge/discharge curves of PUCC at various electrolytes in full cells.

triangular shape for the galvanostatic charge-discharge (GCD) curves of the full cell (Fig. 3d) also demonstrate its EDL-based supercapacitive nature. The relationship of the current ( $i$ ) and the scan rate ( $v$ ) obeys a power-law as  $i = av^b$ , where  $a$  and  $b$  are computable values, which could be achieved *via* the intercept and slope of the  $\log(i)$ - $\log(v)$  plots (Supplementary Fig. 7), respectively. Theoretically, a  $b$ -value of 1.0 and 0.5 means a surface-controlled capacitive process and a diffusion-controlled faradaic intercalation process, respectively. By calculation, the  $b$ -values of the anodic peak and the cathodic peak for the full cell are 0.99 and 0.91, respectively, suggesting a high capacitive contribution. The areal capacitance of the full cell assembled by the PUCC is as high as  $473 \text{ mF cm}^{-2}$  at  $1 \text{ mA cm}^{-2}$ , which is 122 times higher than that of the full cell assembled by the CC (Fig. 3e and Supplementary Fig. 8). High voltage is beneficial for obtaining high capacity and thus high salt adsorption capacity. However, excessively high voltages can exacerbate side reactions, such as water splitting, as shown in Supplementary Fig. 9. In this regard, 1.6 V was chosen for the full cell measurements. The full cell based on the PUCC shows the areal capacitances of 443.4, 327.5, 220.0, and  $122.5 \text{ mF cm}^{-2}$  at 2, 5, 8, and  $10 \text{ mA cm}^{-2}$ , respectively, demonstrating its excellent rate performances. More importantly, except NaCl aqueous solution, the full cell based on the PUCC also shows high capacitances in other aqueous solutions, including  $\text{MgSO}_4$ ,  $\text{CaCl}_2$ , and KCl aqueous solution as well as natural seawater (Fig. 3f). This ion-independent property makes it a promising candidate electrode for seawater CDI.

### CDI performances

To further explore the CDI performances of the PUCC, a CDI cell was assembled, as schematically shown in Fig. 4a. The CDI device was operated on a constant current mode. Each of the adsorption-

desorption measurement was performed until little conductivity change was observed. In the electrochemical salt adsorption process, sodium ions are adsorbed on the anode and chloride ions are adsorbed on the cathode, which lead to a conductivity decrease; while for the electrochemical salt desorption process, the ions are desorbed from the electrodes into the electrolyte solution, causing a conductivity increase. The corresponding salt concentration change vs. time are shown in Fig. 4b. The salt adsorption value for the PUCC is  $31.5 \text{ mg g}^{-1}$  at  $0.1 \text{ mA cm}^{-2}$  in a voltage range of 0–1.6 V (Fig. 4b), corresponding to a high v-SAC of  $13 \text{ mg cm}^{-3}$ , which is 8 times that of the CC. The charge efficiency  $\eta$  is one of the most significant parameters for CDI performances, which represents the ratio of the ionic removal charge from the water to the total electrical charge of the electrode. The charge efficiency is as high as 90% for the PUCC during the salt adsorption process.

The effect of the voltage range, salt concentration, and current density on the g-SAC was also investigated. As shown in Fig. 4c and Supplementary Fig. 10, the g-SAC increases with voltage range and salt concentration, while it decreases with current density. The salt removal capacity is calculated as 19.5, 31.5, and  $33 \text{ mg g}^{-1}$  at the voltage range of 1.4, 1.6, and 1.8 V, respectively. At a larger voltage range, the increase in the electrical charge ( $Q = C \times U$ ) contributes to the g-SAC, but it causes more side reactions. Higher salt concentration with lower resistance can enhance the transport flux of ions<sup>36</sup>, making the g-SAC higher. Higher current density leads to lower electrical charge<sup>37–39</sup> and thus lower g-SAC. The ion removal/release time becomes shorter with increasing current density. The excellent CDI performances of the PUCC were visualized in Fig. 4d. The v-SAC of the PUCC is the highest among binder-free carbon-based 3D electrodes<sup>35,40–43</sup>. The high adsorption capacity can be ascribed to the super-hydrophilic surface and ultramicroporous structures.

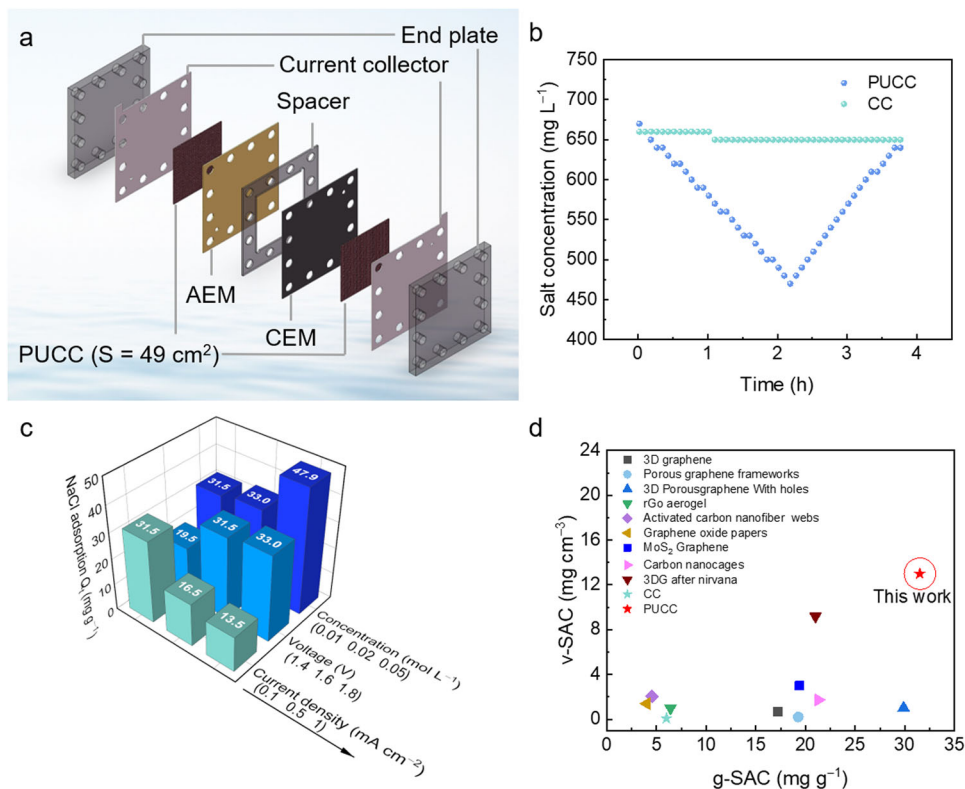


**Fig. 4** The CDI performances of PUCC in NaCl aqueous solution. **a** Schematic diagram of the CDI device. **b** Electro-sorption and electro-desorption process of PUCC and CC at  $0.1 \text{ mA cm}^{-2}$ . **c** The effect of current density, voltage, and initial concentration of the solution on the adsorption capacity. **d** Comparison of g-SAC and v-SAC of the free-standing 3D carbon-based CDI electrodes.

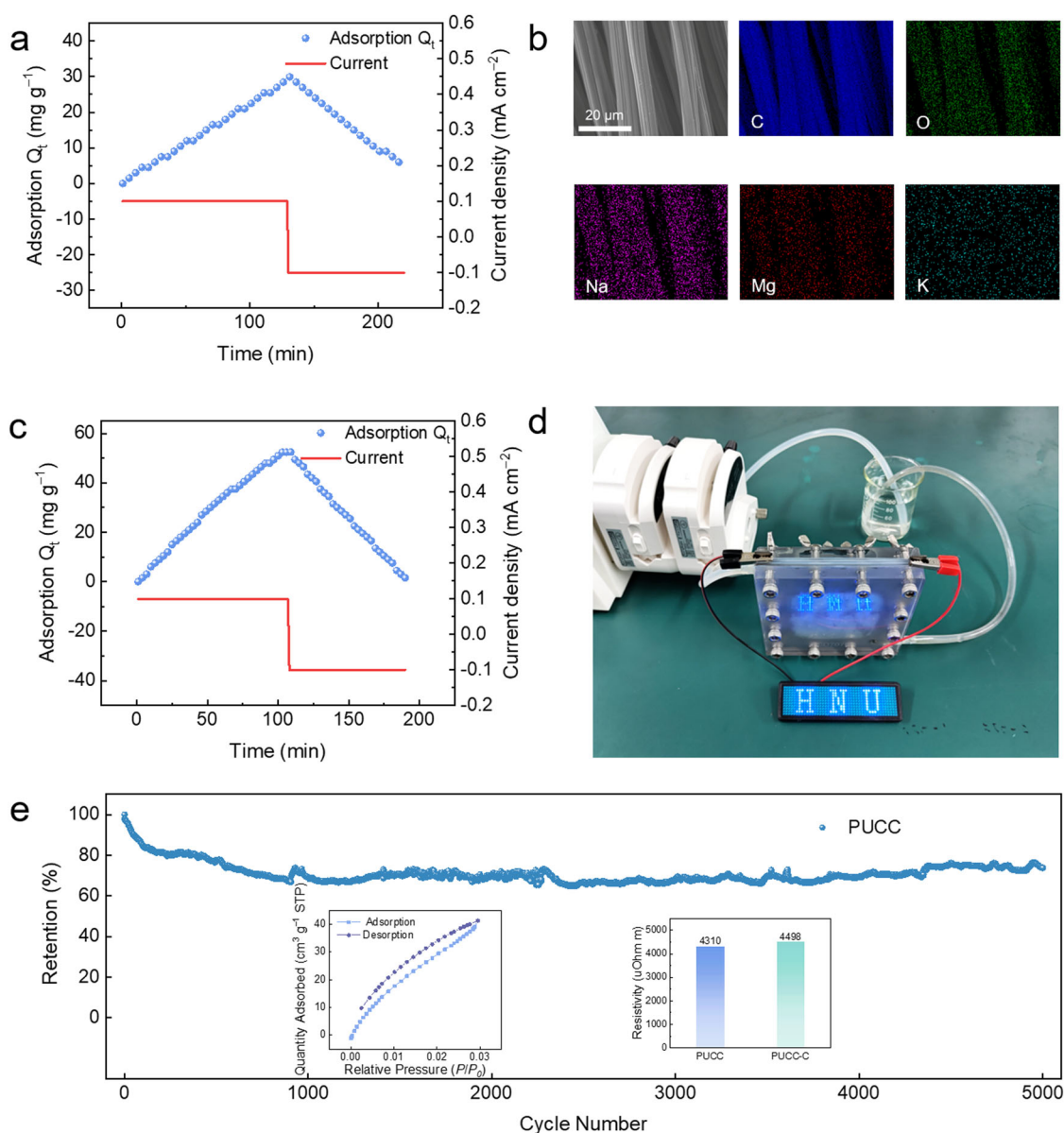


**Fig. 5** The CDI performances of PUC in diluted seawater. **a** An electrosorption-desorption cycle of PUC at  $0.1 \text{ mA cm}^{-2}$ . **b** FESEM image and corresponding elemental mappings of PUC anode after the electrosorption process. **c** The electrosorption-desorption process for two devices connected in series. **d** A LED panel can be lighted by a CDI cell during the ion desorption process. **e** Cycling stability of PUC. The insets in **(e)** show the  $\text{CO}_2$  adsorption/desorption isotherms and resistivity of PUC after the cycle test.

As the desalination function of the PUC is independent of ion types, it is expected that the PUC can be also applied to the desalination of the water with complex ion compositions. As a conceptual presentation, we tested the CDI performances of the PUC in a diluted seawater. To obtain large enough changes in conductivity, the natural seawater was diluted by 50 times before the CDI test. Under a constant current mode, the g-SAC achieves a high value of  $30 \text{ mg g}^{-1}$  (Fig. 5a). After the desalination process, cations, including  $\text{Na}^+$ ,  $\text{Mg}^{2+}$ , and  $\text{K}^+$  are adsorbed on the PUC anode (Fig. 5b), and there are abundant  $\text{Cl}^-$  and  $\text{SO}_4^{2-}$  on the PUC cathode (Supplementary Fig. 11). The EDX mapping results validate the EDLs mechanism for the CDI process. For practical applications, it needs many CDI devices in series connection to meet the required desalination amounts. When two CDI devices are connected in series, they indeed exhibit double desalination amount to that of a CDI device (comparing Fig. 5c with Fig. 5a), demonstrating the application potential. During the desalination

process, electric charge is stored on the electrode and it can be utilized during the ions release process. For example, after the charge process (namely the desalination process), the CDI device can light an LED panel (Fig. 5d).

Cycling lifespan of electrodes is another key parameter for CDI, which determines the desalination costs. Typical carbon materials usually demonstrate dozens of cycles (Supplementary Table 1)<sup>35,42,44–55</sup>. On the contrary, the CDI device based on the PUC electrodes displays stable desalination capability for 5000 cycles, where the retention rate is as high as 74% (Fig. 5e), owing to the pre-oxidized strategy. After 5000 cycles, the microporous surface area still remains at a high level of  $474 \text{ m}^2 \text{ g}^{-1}$  (Fig. 5e). The microporous surface area of the PUC after cycling test is even higher than that of the pristine one, whose exact mechanisms are still unclear and need further investigations. The surface states of the PUC after 5000 cycles are also similar to those of the pristine one (Supplementary Fig. 12). Furthermore, the electrical resistivity

of the PUCC anode only increases by 4.4% (4310 vs. 4498  $\mu\text{Ohm m}$  for the pristine and cycled PUCC), as shown in the inset in Fig. 5e. In addition, the appearances of the ion exchange membranes during the cycling process keep basically unchanged (Supplementary Fig. 13), further verifying the good cycling stability. It is also worth mentioning that the pre-oxidized strategy in the current investigation is universal and can be applied to other carbon materials. For example, the pre-oxidized carbon paper shows more enhanced electrochemical performances than the unmodified carbon paper (Supplementary Fig. 14).

## DISCUSSION

A pre-oxidized strategy was developed to significantly improve the cycling lifespan and salt adsorption capacity of carbon clothes for CDI applications. After the simple pre-oxidized treatment, the PUCC electrode integrates multiple advantages of (1) ultramicro-porous structure; (2) superhydrophilic surface; (3) high electrode tensile strength of 2.6 MPa; (4) pre-oxidized and stable surface; (5) high conductivity compared with power-based electrodes; (6) 100% of active materials/electrode ratio (free of current collector, conductive additive, and binder). Thanks to the above unique characteristics, the PUCC exhibits ultrahigh salt adsorption capacity (13  $\text{mg cm}^{-3}$  and 31.5  $\text{mg g}^{-1}$ ) and ultralong lifespan of 5000 cycles. This work can provide a new avenue to design high-performance, low-cost, and durable electrodes for water treatment and renewable energy in the future.

## METHODS

### Synthesis

The synthesis method was similar to our previous report<sup>56</sup>. Commercial carbon cloth textiles (thickness: 0.33 mm) were purchased from HeSen Co., Ltd (Shanghai, China). The carbon cloth was calcinated at 450 °C for 2 h in air to obtain the pre-oxidized ultramicro-porous carbon cloth.

### Characterizations

The morphologies of the samples were observed by a field emission scanning electron microscope (FESEM, S-4800, Hitachi, Japan) and an aberration-corrected transmission electron microscope (TEM, Titan G2 60-300, FEI Co., Hillsboro, OR). Before the TEM characterizations, the samples were treated by ion milling on a focused ion beam (FIB) in SEM. X-ray diffraction (XRD) measurements were conducted on a XRD-6000 diffractometer (Shimadzu) with Cu K $\alpha$  radiation at 40 kV and 25 mA ( $\lambda = 1.5406 \text{ \AA}$ ). Raman tests were carried out with a Dxr2 xi system (Thermo Fisher Scientific) with a Nd:YAG intracavity doubled laser operated at 532 nm. The X-ray photoelectron spectra (XPS) characterization was carried out on a Escalab Xi+ instrument (Thermo Fisher Scientific, US) with Al K $\alpha$  radiation at 100 eV and 15.0 kV. The base pressure of the analyzer chamber was  $8 \times 10^{-10}$  Pa. The binding energies were calibrated by using the containment carbon at 284.8 eV. The low-temperature N $_2$  adsorption-desorption analysis was performed at 77 K using a Micromeritics ASAP 2020 (Micromeritics Instrument Corp.). Prior to the nitrogen adsorption-desorption measurements, the samples were degassed at 150 °C for 14 h to dislodge the physisorbed gases. The CO $_2$  adsorption-desorption test was performed at a temperature of 273 K. The contact angle tests used the optical contact angle measuring instrument (Kruss DSA100, GRE), which measures the static contact angle using the sessile drop. The tensile test was conducted on a universal testing system (INSTRON 3343, US) according to the test standard of GB/T 3923. The sample size was 20 mm  $\times$  80 mm. The fracture strength and elongation at break of the sample were determined by the spline method. The thermoelectric properties and resistivity of the sample were tested on a

Seebeck coefficient and resistivity test system. The Zeta potential measurements of PUCC in different pH solutions were conducted by a Zeta meter (Anton Paar SurPASS 3).

### Capacitive performance tests

The electrochemical tests were carried out in a conventional three-electrode configuration by a CHI660E electrochemical workstation (Chenhua, China). The Ag/AgCl electrode and Pt electrode were used as the reference electrode and the counter electrode, respectively. The CC and PUCC were used as working electrodes. The electrolyte was 1 M NaCl aqueous solution. Symmetry full cells constructed by two PUCC electrodes were also assembled and measured. The areal capacitance ( $C_A$ ,  $\text{F cm}^{-2}$ ) of the electrode was calculated from the galvanostatic charge/discharge (GCD) curves by Eq. 1 as follows,

$$C_A = \frac{It}{AU} \quad (1)$$

where  $U$  is the potential window (V),  $A$  represents the electrode projected area ( $\text{cm}^2$ ),  $I$  is the current (A), and  $t$  means the discharge time (s).

### CDI tests

The CDI experiments were conducted in a continuously recycling system including a unit cell, a peristaltic pump, conductivity monitor, a tank for the water, and a battery tester (CT2001A, Land) at constant current mode. For the water flow loop, the feed solution was continuously pumped into the unit cell and the effluent was returned to the tank. The feed solution with a volume of 100 mL was NaCl aqueous solution (initial concentration: 10 mM) or diluted seawater (the dilution times is 50 times so that the salinity change in the treated solution was large enough to be measured accurately). The flow rate was 10–100  $\text{mL min}^{-1}$ . The sizes of the electrodes were 7 cm  $\times$  7 cm. The ion exchange membranes were placed in front of each electrode to block the co-ions. The variations in conductivity and voltage were recorded.

The gravimetric salt adsorption capacity ( $g\text{-SAC}$ ,  $\text{mg g}^{-1}$ ) and volumetric salt adsorption capacity ( $v\text{-SAC}$ ,  $\text{mg cm}^{-3}$ ) was calculated by Eqs. 2 and 3 as follows,

$$g\text{-SAC} = \frac{(C_0 - C_e) \times V}{m} \quad (2)$$

$$v\text{-SAC} = \frac{(C_0 - C_e) \times V}{V_e} \quad (3)$$

where  $C_0$  ( $\text{mg L}^{-1}$ ),  $C_e$  ( $\text{mg L}^{-1}$ ), and  $V$  (L) were the initial solution concentration, the solution concentration at equilibrium, and the total volume of the feed solution, respectively. The  $m$  (g) and  $V_e$  ( $\text{cm}^3$ ) mean the mass and volume of the electrode, respectively.

The charge efficiency ( $\eta$ ) at one cycle was examined by Eq. 4 as follows,

$$\eta(\%) = \frac{g\text{-SAC}}{M_w} \times \frac{F}{\int I dt} \times 100 \quad (4)$$

where  $F$  represents the faradaic constant ( $96485 \text{ C mol}^{-1}$ ),  $I$  is the applied current (A), and  $M_w$  is the molecular weight of NaCl ( $58.44 \text{ g mol}^{-1}$ ).

### DATA AVAILABILITY

All data generated or analysed in this study are included in this published article and its Supplementary Information files.

Received: 29 July 2023; Accepted: 20 October 2023;

Published online: 31 October 2023

## REFERENCES

- Rodell, M. et al. Emerging trends in global freshwater availability. *Nature* **557**, 651–659 (2018).
- Shannon, M. A. et al. Science and technology for water purification in the coming decades. *Nature* **452**, 301–310 (2008).
- He, C. et al. Future global urban water scarcity and potential solutions. *Nat. Commun.* **12**, 1–11 (2021).
- Cao, Z. et al. Ultrathin ZSM-5 zeolite nanosheet laminated membrane for high-flux desalination of concentrated brines. *Sci. Adv.* **4**, 1–10 (2018).
- Alkhubiri, A., Darwish, N. & Hilal, N. Membrane distillation: a comprehensive review. *Desalination* **287**, 2–18 (2012).
- Nassrullah, H., Anis, S. F., Hashaikeh, R. & Hilal, N. Energy for desalination: a state-of-the-art review. *Desalination* **491**, 114569 (2020).
- Zhao, S. et al. Engineering antifouling reverse osmosis membranes: a review. *Desalination* **499**, 114857 (2021).
- Srimuk, P., Su, X., Yoon, J., Aurbach, D. & Presser, V. Charge-transfer materials for electrochemical water desalination, ion separation and the recovery of elements. *Nat. Rev. Mater.* **5**, 517–538 (2020).
- Porada, S., Zhao, R., Van Der Wal, A., Presser, V. & Biesheuvel, P. M. Review on the science and technology of water desalination by capacitive deionization. *Prog. Mater. Sci.* **58**, 1388–1442 (2013).
- Hawks, S. A. et al. Performance metrics for the objective assessment of capacitive deionization systems. *Water Res.* **152**, 126–137 (2019).
- Liu, T. et al. Exceptional capacitive deionization rate and capacity by block copolymer-based porous carbon fibers. *Sci. Adv.* **6**, eaaz0906 (2020).
- Bao, W. et al. Porous Cryo-Dried MXene for efficient capacitive deionization. *Joule* **2**, 778–787 (2018).
- Tang, K., Hong, T. Z. X., You, L. & Zhou, K. Carbon–metal compound composite electrodes for capacitive deionization: synthesis, development and applications. *J. Mater. Chem. A* **7**, 26693–26743 (2019).
- Gao, X., Omosebi, A., Landon, J. & Liu, K. Surface charge enhanced carbon electrodes for stable and efficient capacitive deionization using inverted adsorption–desorption behavior. *Energy Environ. Sci.* **8**, 897–909 (2015).
- Lee, J. et al. Rocking-chair capacitive deionization for continuous Brackish water desalination. *ACS Sustain. Chem. Eng.* **6**, 10815–10822 (2018).
- Jain, A. et al. Aqueous-processed, high-capacity electrodes for membrane capacitive deionization. *Environ. Sci. Technol.* **52**, 5859–5867 (2018).
- Zhang, X. Y. & Dutta, J. X-Fe (X = Mn, Co, Cu) Prussian Blue Analogue-modified carbon cloth electrodes for capacitive deionization. *ACS Appl. Energy Mater.* **4**, 8275–8284 (2021).
- Yasin, A. S., Mohamed, I. M. A., Mousa, H. M., Park, C. H. & Kim, C. S. Facile synthesis of TiO<sub>2</sub>/ZrO<sub>2</sub> nanofibers/nitrogen co-doped activated carbon to enhance the desalination and bacterial inactivation via capacitive deionization. *Sci. Rep.* **8**, 541 (2018).
- Chen, F. et al. Dual-ions electrochemical deionization: a desalination generator. *Energy Environ. Sci.* **10**, 2081–2089 (2017).
- Wei, W., Gu, X., Wang, R., Feng, X. & Chen, H. Wood-based self-supporting nanoporous three-dimensional electrode for high-efficiency battery deionization. *Nano Lett.* **22**, 7572–7578 (2022).
- Wei, W. et al. Electrochemical driven phase segregation enabled dual-ion removal battery deionization electrode. *Nano Lett.* **21**, 4830–4837 (2021).
- Singh, K. et al. Divalent ion selectivity in capacitive deionization with Vanadium Hexacyanoferrate: experiments and quantum-chemical computations. *Adv. Funct. Mater.* **31**, 2105203 (2021).
- Wang, H. et al. Ultramicroporous carbon cloth for flexible energy storage with high areal capacitance. *Energy Storage Mater.* **7**, 216–221 (2017).
- Chmiola, J. et al. Anomalous increase in carbon at pore sizes less than 1 nanometer. *Science* **313**, 1760–1763 (2006).
- Zhang, Y. et al. Ionophobicity of carbon sub-nanometer pores enables efficient desalination at high salinity. *Cell Rep. Phys. Sci.* **3**, 100689 (2022).
- Li, Z. et al. Tuning the interlayer spacing of graphene laminate films for efficient pore utilization towards compact capacitive energy storage. *Nat. Energy* **5**, 160–168 (2020).
- Bu, Y. et al. Compressing carbon nanocages by capillarity for optimizing porous structures toward ultrahigh-volumetric-performance supercapacitors. *Adv. Mater.* **29**, 1700470 (2017).
- Hand, S., Guest, J. S. & Cusick, R. D. Technoeconomic analysis of Brackish water capacitive deionization: navigating tradeoffs between performance, lifetime, and material costs. *Environ. Sci. Technol.* **53**, 13353–13363 (2019).
- Liu, X., Shanbhag, S., Natesakhawat, S., Whitacre, J. F. & Mauter, M. S. Performance loss of activated carbon electrodes in capacitive deionization: mechanisms and material property predictors. *Environ. Sci. Technol.* **54**, 15516–15526 (2020).
- Zhang, C., He, D., Ma, J., Tang, W. & Waite, T. D. Faradaic reactions in capacitive deionization (CDI) - problems and possibilities: a review. *Water Res.* **128**, 314–330 (2018).
- Cohen, I., Avraham, E., Bouhadana, Y., Soffer, A. & Aurbach, D. Long term stability of capacitive de-ionization processes for water desalination: the challenge of positive electrodes corrosion. *Electrochim. Acta* **106**, 91–100 (2013).
- Gao, X., Omosebi, A., Landon, J. & Liu, K. Dependence of the capacitive deionization performance on potential of zero charge shifting of carbon xerogel electrodes during long-term operation. *J. Electrochem. Soc.* **161**, E159–E166 (2014).
- Wu, M. et al. Metallic 1T MoS<sub>2</sub> nanosheet arrays vertically grown on activated carbon fiber cloth for enhanced Li-ion storage performance. *J. Mater. Chem. A* **5**, 14061–14069 (2017).
- Yang, D. et al. Chemical analysis of graphene oxide films after heat and chemical treatments by X-ray photoelectron and Micro-Raman spectroscopy. *Carbon* **47**, 145–152 (2009).
- Li, Y. et al. Reborn three-dimensional graphene with ultrahigh volumetric desalination capacity. *Adv. Mater.* **33**, 2105853 (2021).
- Hamid Elsheikh, M. et al. A review on thermoelectric renewable energy: principle parameters that affect their performance. *Renew. Sustain. Energy Rev.* **30**, 337–355 (2014).
- Wen, W., Wu, J. M., Jiang, Y. Z., Lai, L. L. & Song, J. Pseudocapacitance-enhanced Li-Ion microbatteries derived by a TiN@TiO<sub>2</sub> nanowire anode. *Chem* **2**, 404–416 (2017).
- Geng, C. et al. Surface-induced desolvation of hydronium ion enables anatase TiO<sub>2</sub> as an efficient anode for proton batteries. *Nano Lett.* **21**, 7021–7029 (2021).
- Wen, W. et al. Univariate lattice parameter modulation of single-crystal-like anatase TiO<sub>2</sub> hierarchical nanowire arrays to improve photoactivity. *Chem. Mater.* **33**, 1489–1497 (2021).
- Zhang, H. et al. Preparation and characterization of colorful graphene oxide papers and flexible N-doping graphene papers for supercapacitor and capacitive deionization. *Carbon Energy* **2**, 656–674 (2020).
- Zhang, M. et al. Robust graphene composite films for multifunctional electrochemical capacitors with an ultrawide range of areal mass loading toward high-rate frequency response and ultrahigh specific capacitance. *Energy Environ. Sci.* **11**, 559–565 (2018).
- Han, J. et al. Capacitive deionization of saline water by using MoS<sub>2</sub>-graphene hybrid electrodes with high volumetric adsorption capacity. *Environ. Sci. Technol.* **53**, 12668–12676 (2019).
- Zang, X. et al. Enhanced electrosorption ability of carbon nanocages as an advanced electrode material for capacitive deionization. *ACS Appl. Mater. Interfaces* **12**, 2180–2190 (2020).
- Li, M. & Park, H. G. Pseudocapacitive coating for effective capacitive deionization. *ACS Appl. Mater. Interfaces* **10**, 2442–2450 (2018).
- Che, X. et al. Inverted capacitive deionization with highly enhanced stability performance utilizing ionic liquid-functionalized carbon electrodes. *ACS Sustain. Chem. Eng.* **7**, 15715–15722 (2019).
- Wu, Q. et al. Novel inorganic integrated membrane electrodes for membrane capacitive deionization. *ACS Appl. Mater. Interfaces* **13**, 46537–46548 (2021).
- Wang, X. R. et al. Hierarchical MXene/Polypyrrole-decorated carbon nanofibers for asymmetrical capacitive deionization. *ACS Appl. Mater. Interfaces* **14**, 53150–53164 (2022).
- Wu, T. et al. Starch derived porous carbon nanosheets for high-performance photovoltaic capacitive deionization. *Environ. Sci. Technol.* **51**, 9244–9251 (2017).
- Tang, K. et al. Macropore- and micropore-dominated carbon derived from poly(vinyl alcohol) and polyvinylpyrrolidone for supercapacitor and capacitive deionization. *ACS Sustain. Chem. Eng.* **5**, 11324–11333 (2017).
- Wang, H. et al. Hierarchical porous carbon from the synergistic ‘pore-on-pore’ strategy for efficient capacitive deionization. *ACS Sustain. Chem. Eng.* **8**, 1129–1136 (2020).
- Lado, J. J., Zornitta, R. L., Vázquez Rodríguez, I., Malverdi Barcelos, K. & Ruotolo, L. A. M. Sugarcane biowaste-derived biochars as capacitive deionization electrodes for Brackish water desalination and water-softening applications. *ACS Sustain. Chem. Eng.* **7**, 18992–19004 (2019).
- Szabó, L. et al. Tailoring the structure of chitosan-based porous carbon nanofiber architectures toward efficient capacitive charge storage and capacitive deionization. *ACS Appl. Mater. Interfaces* **14**, 4004–4021 (2022).
- Shi, W. et al. Bismuth nanoparticle-embedded porous carbon frameworks as a high-rate chloride storage electrode for water desalination. *ACS Appl. Mater. Interfaces* **13**, 21149–21156 (2021).
- Zhang, D. et al. Enhanced capacitive deionization performance of graphene/carbon nanotube composites. *J. Mater. Chem.* **22**, 14696–14704 (2012).
- Zhao, W. et al. Dual-Ion electrochemical deionization system with binder-free aerogel electrodes. *Small* **15**, 1805505 (2019).
- Gu, Y. J., Wen, W. & Wu, J. M. Simple air calcination affords commercial carbon cloth with high areal specific capacitance for symmetrical supercapacitors. *J. Mater. Chem. A* **6**, 21078–21086 (2018).

## ACKNOWLEDGEMENTS

This work was financially supported by the Hainan Provincial Natural Science Foundation of China (No. 521RC740 and 2019RC047) and National Natural Science Foundation of China (No. 52362030, 51862005 and 52201211).

## AUTHOR CONTRIBUTIONS

X.Z. — Conceptualization, Material preparation, Measurement, Writing original draft; Y.Z. — Methodology, Measurement, Investigation; Z.Z., Z.G., T.S., J.Q., N.Q. and Z.Z. — Measurement, Investigation; W.W. — Conceptualization, Supervision, Reviewing and Editing, Project administration.

## COMPETING INTERESTS

The authors declare no competing interests.

## ADDITIONAL INFORMATION

**Supplementary information** The online version contains supplementary material available at <https://doi.org/10.1038/s41545-023-00289-z>.

**Correspondence** and requests for materials should be addressed to Wei Wen.

**Reprints and permission information** is available at <http://www.nature.com/reprints>

**Publisher's note** Springer Nature remains neutral with regard to jurisdictional claims in published maps and institutional affiliations.



**Open Access** This article is licensed under a Creative Commons Attribution 4.0 International License, which permits use, sharing, adaptation, distribution and reproduction in any medium or format, as long as you give appropriate credit to the original author(s) and the source, provide a link to the Creative Commons license, and indicate if changes were made. The images or other third party material in this article are included in the article's Creative Commons license, unless indicated otherwise in a credit line to the material. If material is not included in the article's Creative Commons license and your intended use is not permitted by statutory regulation or exceeds the permitted use, you will need to obtain permission directly from the copyright holder. To view a copy of this license, visit <http://creativecommons.org/licenses/by/4.0/>.

© The Author(s) 2023